

Research Article

Introducing Ce ions and oxygen vacancies into VO₂ nanostructures with high specific surface area for efficient aqueous Zn-ion storage

 Mingying Bao^a, Zhengchunyu Zhang^a, Xuguang An^b, Baojuan Xi^a, Shenglin Xiong^{a,*}
^a Key Laboratory of Colloid and Interface Chemistry, Ministry of Education, School of Chemistry and Chemical Engineering, State Key Laboratory of Crystal Materials, Shandong University, Jinan 250100, China

^b School of Mechanical Engineering, Chengdu University, Chengdu 610106, China

ARTICLE INFO

Keywords:

 Cathode
 Ce ions
 Oxygen vacancies
 Ce-VO₂
 Aqueous Zn-ion batteries

ABSTRACT

Positive electrodes play a decisive role in exploring the Zn²⁺ storage mechanism and improving the electrochemical performance of aqueous Zn-ion batteries (AZIBs). Feasible design and preparation of cathode materials have been crucial for AZIBs in recent years. Herein, taking the advantage of the tunnel structure of VO₂, which can withstand volume change during charging/discharging, VO₂ doped with Ce ions is synthesized by a simple one-step hydrothermal method and oxygen vacancies are synchronously generated during synthesis. It delivers a capacity of 158.5 mAh g⁻¹ at the current density of 5 A g⁻¹ after 1000 cycles and exhibits an excellent energy density of 312.8 Wh kg⁻¹ at the power density of 142 W kg⁻¹. The structural modification and prospect of enhancing its conductivity by doping with rare-earth metals and introducing oxygen vacancies may aid in improving the stability of AZIBs in the future.

1. Introduction

In 2020, the Chinese government put forward a “carbon neutrality and carbon peaking” policy. Energy conservation, emission reduction, and green economy assert in improving and sustaining the environment [1-2]. Considering this background and to store renewable energy, efficient and clean electrochemical battery technologies should be developed [3-5]. Li-ion batteries (LIBs) have greatly facilitated our daily life since their successful commercialization and have been widely applied in multiple fields as dominant energy storage devices [6-8]. Nonetheless, LIBs suffer from high cost, unsustainable long cycling, and risk of leakage, which prompt the need to search for other alternative efficient energy storage systems [9-11]. Among various candidates, aqueous Zn-ion batteries (AZIBs) are a potential alternative for new secondary batteries powered by clean energy owing to their characteristics of high safety, high theoretical specific capacity (5851 mA g⁻¹), convenient assembly, high crustal abundance of Zn, and excellent fit between Zn and aqueous solutions (moderate reactivity and low redox potential) [12-15].

The exploration of cathode materials is significant for investigating energy-storage mechanisms and improving the electrochemical performance of AZIBs, which requires designing materials with high stability and performance [16-18]. In the recent years, several kinds of materials, including V-based oxides, manganese oxides, metal-organic frameworks, and covalent organic frameworks, have been explored [19-22].

Among these materials, VO₂ cathode has attracted conspicuous attention owing to their high theoretical specific capacity and abundance [23,24]. In terms of reported works, the tunnel structure of VO₂ is constructed by strong covalent bonds, which are more solid and stable than the layered structure connected by weak van der Waals forces [25,26]. Moreover, the large tunnel structure (4.984 Å × 3.281 Å) can accommodate Zn²⁺ (0.74 Å) and withstand the volume change caused by the insertion/extraction of Zn²⁺ [27,28]. Doping of exogenous elements can address the poor electrical conductivity of VO₂, and nanostructured materials with large specific surface areas can enhance the capacity to store charges [29]. However, as previous researchers mainly focus on transition metals or alkali (earth) metals based on doping optimization, imperative breakthroughs in the field of rare-earth metals remain limited [30,31]. Moreover, rare-earth metal cerium has been proposed to better support the structure of V-based compounds with large ionic radii. Therefore, cerium can be employed as an exogenous element to construct an efficient and stable positive-electrode material for AZIBs.

Herein, Ce-doped VO₂ (Ce-VO₂) was synthesized by a simple one-step hydrothermal method. Moreover, the introduction of exogenous elements prompted generating oxygen vacancies in the synthesis process. A series of experimental tests confirmed the significant improvement in the storage capacity of Zn²⁺ with Ce-VO₂ as the positive electrode of AZIBs. Specifically, Ce doping changed the local electronic structure of VO₂ and further improved its conductivity. Nanostructures with large

* Corresponding author.

 E-mail address: chexsl@sdu.edu.cn (S. Xiong).

<https://doi.org/10.1016/j.chphma.2024.05.004>

Received 28 March 2024; Received in revised form 26 May 2024; Accepted 27 May 2024

Available online 14 June 2024

 2772-5715/© 2024 The Authors. Publishing Services by Elsevier B.V. on behalf of KeAi Communications Co. Ltd. This is an open access article under the CC BY license (<http://creativecommons.org/licenses/by/4.0/>)

specific surface areas play an important role in decreasing the diffusion distance and accelerating the diffusion kinetics of guest ions, which are instrumental in Zn^{2+} insertion/extraction. A stable structure can alleviate the volume change during charging/discharging. In addition, the presence of oxygen vacancies enhances the reactivity and weakens the interaction between the electrode material and guest ions, which is conducive to improving the electrochemical specific capacity. Compared with pure VO_2 , the Ce-VO_2 electrode material exhibited exceptionally prolonged cycling stability (158.5 mAh g^{-1} at the current density of 5 A g^{-1} after 1000 cycles) and good rate performance, and provided an excellent energy density of 312.8 Wh kg^{-1} at the power density of 142 W kg^{-1} . This method provides a new method to optimize cathode materials for AZIBs in the future.

2. Experimental section

2.1. Sample preparation

Ce-VO_2 was synthesized by a simple one-step hydrothermal method. First, $3.3 \text{ mmol V}_2\text{O}_5$ (Aladdin, AR, 99.0%) was dissolved in 10 mL deionized water, resulting in solution A. Meanwhile, $9.5 \text{ mmol C}_2\text{H}_2\text{O}_4 \cdot 2\text{H}_2\text{O}$ (Sinopharm Chemical Reagent Limited Corporation, AR) was added to 10 mL deionized water, which is denoted as solution B. After complete dissolution, two solutions were mixed and stirred for 10 min at room temperature. Under magnetic stirring, a uniform dark blue solution was obtained at $80 \text{ }^\circ\text{C}$ after 30 min , followed by the addition of $0.0876 \text{ g Ce(NO}_3)_3 \cdot 6\text{H}_2\text{O}$ (Shanghai Macklin reagent, AR, 99.5%). Subsequently, 50 mL anhydrous ethanol (Sinopharm Chemical Reagent Limited Corporation, AR) was added to the mixed solution and stirred for 0.5 h , transferred into a 100 mL Teflon-lined stainless-steel autoclave and treated at $180 \text{ }^\circ\text{C}$ for 24 h . After completing the reaction, a blue-black precipitate was obtained by washing twice with deionized water and ethanol. Finally, the precipitate was dried in a vacuum oven at $60 \text{ }^\circ\text{C}$, and Ce-VO_2 was obtained. Pure VO_2 was obtained by following a similar procedure without $\text{Ce(NO}_3)_3 \cdot 6\text{H}_2\text{O}$ and anhydrous ethanol added.

2.2. Material characterization

The morphology of the samples was determined by field-emission scanning electron microscopy (Gemini-300, Zeiss) and transmission electron microscopy (TEM, JEM-1011, JEOL). The crystal structures of the samples were obtained by X-ray powder diffractometer (XRD, Cu $K\alpha$, $\lambda = 1.5418 \text{ \AA}$) within the scanning range of 10° – 60° . The Brunauer–Emmett–Teller (BET) specific surface areas, pore volumes, and pore-size distributions of the materials were obtained using an Autosorb-6B instrument at 77 K . Raman spectra were obtained using a Senterra Spectrometer (Bruker). Electron spin resonance (EPR) was tested in the X band with a modulation amplitude of 5.00 G . X-ray photoelectron spectroscopy (XPS, Thermo ESCALAB 250Xi) was also conducted with Al $K\alpha$ ($h\nu = 1486.6 \text{ eV}$).

2.3. Electrochemical characterization

Positive electrodes were prepared by the following steps. Firstly, Ce-VO_2 , acetylene black (conductive agent) and polyvinylidene fluoride (binder) were mixed at a ratio of $7:2:1$. Subsequently, N-methyl-2-pyrrolidone reagent was added as a solvent and ground for 3 h to obtain an evenly mixed slurry. The slurry was then applied to a Ti foil (thickness: 0.02 mm) and dried overnight in the vacuum oven at $80 \text{ }^\circ\text{C}$. Subsequently, the Ti foil coated with the areal loading of active material at 0.8 – 1 mg cm^{-2} was evenly cut into circular disks with a diameter of 12 mm . The Zn foil anode was also divided into a circular disk with a diameter of 14 mm . The CR2016 coin batteries were assembled in air with glass fiber as the separator and 2 M ZnSO_4 aqueous solution as the electrolyte. The electrochemical performance of the batteries was tested

using a battery test system (LAND CT2001A). Cyclic voltammetry (CV) was performed using an electrochemical workstation (CHI 760E, Shanghai Chen Hua) within a voltage window of 0.2 – 1.6 V vs. Zn^{2+}/Zn .

3. Results and discussion

3.1. Phase characterization of Ce-VO_2

Ce-VO_2 was synthesized by a one-step hydrothermal method (Fig. 1(a)). A series of morphological characterization methods (FESEM and TEM images) were performed to clearly observe the microstructure of Ce-VO_2 . Figs. 1(b)(c) show the morphological characteristics of intricately stacked nanostrips with a uniform profile. The TEM image (Fig. 1(d)) shows that Ce-VO_2 is a nanostrip with a length of $\sim 450 \text{ nm}$ and width of $\sim 60 \text{ nm}$. Energy-dispersive X-ray spectroscopy (EDS) was used to determine the elemental distribution. Fig. 1(e) shows the even distribution of V, O, and Ce in Ce-VO_2 , indicating the successful predop- ing of Ce ions in the VO_2 nanostrips.

A series of characterization tests were carried out to determine the phase of the sample. The results are shown in Fig. 2. When selecting the XRD scanning speed, the specific experimental requirements should be considered to achieve the best experimental results. A scanning speed of $30 \text{ }^\circ/\text{min}$ provides a high resolution and good peak shape, which are important for experiments that require high accuracy. Fig. 2(a) shows the XRD pattern of Ce-VO_2 , whereby the diffraction peaks of the sample are consistent with that of the standard card (PDF#31–1438). Moreover, no obvious unusual peak signals of impurities are observed, confirming the crystal structure of the VO_2 powder. Fig. 2(b) shows the Raman spectrum of Ce-VO_2 in the range of 100 – 1100 cm^{-1} . The peaks at 135.3 and 186.8 cm^{-1} are closely related to the bending vibration of the Ce-VO_2 skeleton and those at 279.0 and 404.4 cm^{-1} can be attributed to bending vibration of V=O . The diffraction peak at 691 cm^{-1} is related to the stretching vibration of V-O-V and that at 988.2 cm^{-1} corresponds to the stretching vibration of V=O [32]. In addition, the signal of Ce-VO_2 (isotropic g value is 1.95) was detected by EPR imaging (Fig. 2(c)), which directly confirms the presence of anion vacancy in the Ce-VO_2 [33–35].

High-resolution XPS was used to determine the elemental and valence composition of Ce-VO_2 and pure VO_2 samples. The O 1s spectrum (Fig. 2(d)) can be divided into two characteristic peaks at 530.4 and 531.9 eV , corresponding to the V-O bonds and oxygen vacancies, respectively. Fig. 2(e) shows the high-resolution XPS spectra of V 2p with two peaks at the binding energy of 517.1 and 524.2 eV attributed to V^{4+} , whereas two signal peaks at 516 and 522.8 eV demonstrate the presence of V^{3+} . The coexistence of the mixed valences of vanadium is ascribed to the embedding of Ce^{3+} in the lower valence state, resulting in the partial reduction of V^{4+} to V^{3+} , and the coexistence of $\text{V}^{3+}/\text{V}^{4+}$ can improve the conductivity of the electrode material [36]. The two peaks at 518.1 and 525.4 eV indicate the presence of V^{5+} , which is ascribed to the large specific surface area of the nanomaterials, making it easy to interact with O_2 in the air, thereby oxidizing V. For the V 2p spectrum, the XPS results of the Ce 3d spectrum shown in Fig. 2(f) indicate the partial oxidation of Ce^{3+} to Ce^{4+} , demonstrating the successful pre-embedding of Ce.

The specific surface area and pore size are important parameters of the positive electrode material of Zn-ion batteries. Therefore, the porous structure of Ce-VO_2 and pure VO_2 was characterized by N_2 sorption isotherms method at 77 K , as shown in Fig. S1. According to previous reports, these samples have type IV adsorption/desorption isotherm curves and a mesoporous hysteresis loop within the relative pressure (P/P_0) range of 0.8 – 0.9 , indicating the mesoporous characteristics of these materials [37]. According to the test results, the BET specific surface area of the Ce-VO_2 sample is $196 \text{ m}^2 \text{ g}^{-1}$ (Fig. S1(a)), which is higher than that of pure VO_2 ($123.2 \text{ m}^2 \text{ g}^{-1}$, Fig. S1(c)). In addition, according to the pore-size distribution, the average pore size of Ce-VO_2 is 5.6 nm , which is larger than that of the contrast sample (4.1 nm).

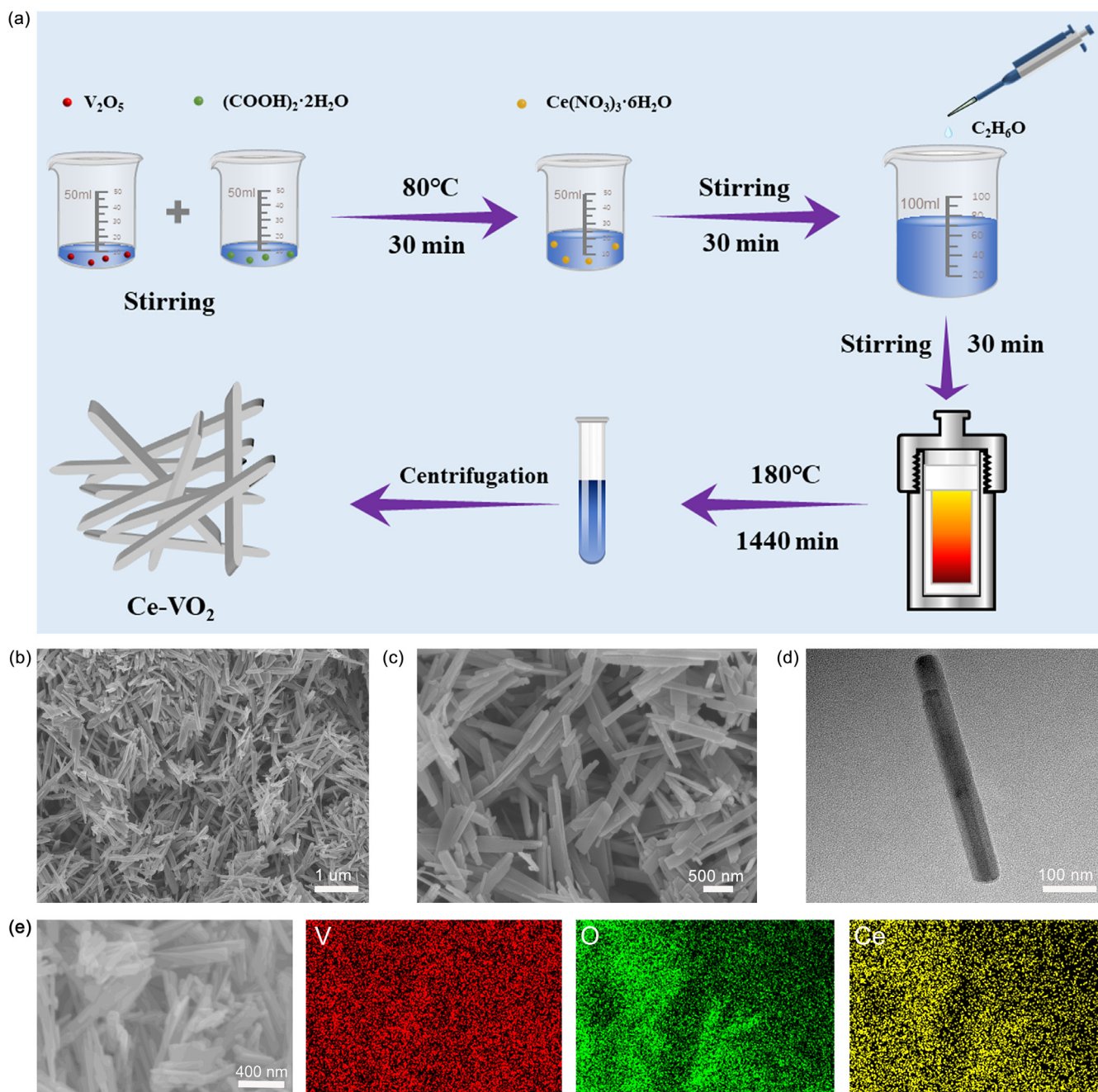


Fig. 1. Morphology and structure characterization of Ce-VO₂ samples: (a) Synthesis diagram. (b)(c) FESEM images. (d) TEM image. (e) EDS mapping images of V, O, and Ce.

Moreover, macropores larger than 50 nm exist in the Ce-VO₂ and VO₂ samples (Figs. S1(b)(d)), confirming that the structures of both samples comprised mesopores (2–50 nm) and macropores. Moreover, the pore volume of Ce-VO₂ (0.477 cm³ g⁻¹) is three times larger than that of VO₂ (0.149 cm³ g⁻¹). Such large specific surface area and pore size are conducive to providing more active sites and shortening the ion diffusion and transfer path, which promotes the electrochemical performance of Ce-VO₂ electrode [38].

3.2. Electrochemical properties of Ce-VO₂

Zn/Ce-VO₂ and Zn/VO₂ coin cells were assembled using 2 M ZnSO₄ solution as the electrolyte to clearly explore the electrochemical properties of Ce-VO₂ electrode. At the same scan rate, the CV curves of the Ce-VO₂ electrode is higher than that of VO₂ (Fig. 3(a)), indicating that

Ce-VO₂ active materials provide higher capacity owing to their large specific surface area and stable structure, thereby facilitating full contact with the electrolyte. In Fig. 3(a), the two peaks represent the stepwise insertion of zinc and hydrogen ions, respectively. The galvanostatic charge–discharge (GCD) curve of Ce-VO₂ at 0.5 A g⁻¹ is displayed in Fig. 3(b). Notably, the Coulombic efficiency of the electrode at a low current is approximately 100%, exhibiting slight capacity fading after 20 cycles. In contrast, the capacity of pure VO₂ declines (Fig. S2), and the charging curve after 20 cycles exhibits a significant difference from the original one, which can be ascribed to the formation of byproducts, resulting in structural collapse and further affecting the Zn²⁺ storage capacity of the VO₂ materials. Electrochemical impedance spectroscopy (EIS, Fig. S3) further monitored the resistances of the two electrodes. Specifically, the semicircle of the Ce-VO₂ electrode is smaller than that of pure VO₂. The charge transfer resistance (R_{ct}) of the cell assembled

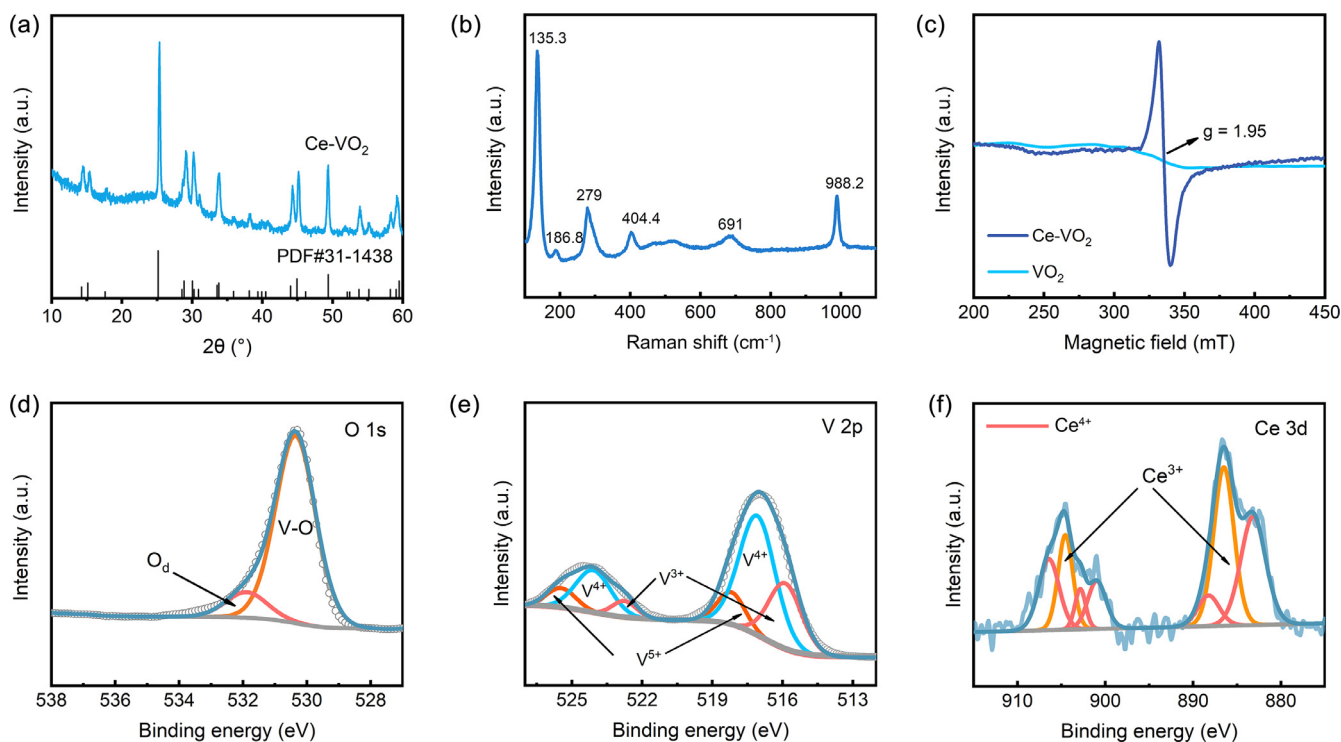


Fig. 2. Structural characterization of the Ce-VO₂ sample: (a) XRD pattern, (b) Raman spectrum, (c) EPR spectra, (d) V 2p and (e) O 1s, and (f) Ce 3d high-resolution XPS spectra.

with Ce-VO₂ (102.9 Ω) is lower than that of VO₂ (368.4 Ω), indicating that Ce-VO₂ cathode can obtain higher conductivity with the optimization of exogenous elements and oxygen vacancies, thereby achieving improved electrochemical performance.

The stable cycling behavior of the Ce-VO₂ electrode at 3 A g⁻¹ is displayed in Fig. 3(c). The fresh electrode is activated by cycling at a low current of 0.3 A g⁻¹ to ensure the realization of the subsequent reaction. The Ce-VO₂ cathode delivers a capacity of 143.2 mAh g⁻¹ after 500 cycles. Ce doping and oxygen defects strengthened the structure. In addition, the change of the local electron cloud enhances the conductivity, and the large specific surface area is conducive to Zn²⁺ migration kinetics. Consequently, the Ce-VO₂ electrode could better adapt to the volume change caused by Zn²⁺ insertion/extraction.

Comparing the rate performance of Ce-VO₂ and VO₂ electrodes in Fig. 3(d), the former has higher and more stable specific capacity under different currents than the latter. Specifically, at the current density of 0.2, 0.4, 0.6, 0.8, 1.0, 2.0, 4.0, 6.0, 8.0, and 10.0 A g⁻¹, the average reversible capacity of the Ce-VO₂ electrode is 465.2, 420.9, 382.2, 356.4, 327.6, 302.4, 282, 252.3, 233.1, and 195.1 mAh g⁻¹, respectively. Furthermore, the specific capacity can recover to 409.5 mAh g⁻¹ as the current density is restored to 0.4 A g⁻¹, depicting a capacity retention of 97.3%. In contrast, the rate performance of the VO₂ cathode material displays an obvious instability tendency. In addition, the capacity retention is only 87%, suggesting the certain hysteresis of the VO₂ electrode. Moreover, capacity of the Ce-VO₂ electrode is 195.1 mAh g⁻¹ at a high current density of 10 A g⁻¹, whereas that of the VO₂ electrode is only 60 mAh g⁻¹, indicating that the capacity of the Ce-VO₂ electrode is approximately three times that of pure VO₂ electrode. The outstanding rate performance verifies the excellent storage capacity of Zn²⁺ using the Ce-VO₂. Meanwhile, the introduction of Ce and oxygen vacancies can regulate the microstructure of cathode materials and improve the conductivity of the electrode, while enhancing the reaction kinetics, which are important factors for promoting the excellent rate performance.

Fig. 3(e) displays the GCD plots of the Ce-VO₂ electrode at different current densities. The capacity gradually decreases with increasing

current density, and two voltage plateaus with similar shapes are maintained in the cycling process, indicating the fast diffusion dynamics of Zn²⁺ during the charge/discharge process. The GCD plots corresponding to the rate test of the pure VO₂ electrode are shown in Fig. S4, which depicts a lower capacity than that of the Ce-VO₂ electrode. The shape of the GCD curves changed significantly as the current is increased. The results highlight the significant decline in the capacity of pure VO₂ during the de(inter)calation) of Zn²⁺ owing to its low conductivity and poor structural reversibility. The power density of the electrode is notable compared with other previously reported V-based materials (Fig. 3(f)) [39–44]. The energy density of the Ce-VO₂ cathode gradually increases with the power density. Specifically, the Ce-VO₂ electrode achieves high energy densities of 312.8 Wh kg⁻¹ at a lower power density of 142 W kg⁻¹ and 106 Wh kg⁻¹ at a higher power density of 5112 W kg⁻¹, indicating the competitive advantages of the Ce-VO₂ electrode and its potential development prospect for future electrochemical energy-storage systems.

The electrochemical cycling performance of the Ce-VO₂ electrode was further tested at 5 A g⁻¹ to prove its charge/discharge stability, as shown in Fig. 3(g). An impressive capacity of 158.5 mAh g⁻¹ is achieved after 1000 cycles with a slight decay trend, whereas the VO₂ electrode has a poor cycling performance. Fig. 3(h) shows the EPR spectra of the Ce-VO₂ electrode cycled at different stages of fully charged states at 5 A g⁻¹. The oxygen vacancy in the sample structure nearly remain unchanged, indicating that the structure of Ce-VO₂ is relatively stable during the cycling process with the capability of supporting Zn²⁺ insertion/extraction under a high current density ensuring long-term cyclic stability.

3.3. Electrochemical kinetic behavior of Ce-VO₂ cathode

CV and galvanostatic intermittent titration technique (GITT) were performed to further analyze the kinetic behavior of Zn²⁺ in the electrode. According to the CV curves at different sweeping rates (Fig. 4(a)), the curves maintain a similar shape with a gradual increase in the area. The notable oxidation peaks move towards higher potentials, and the

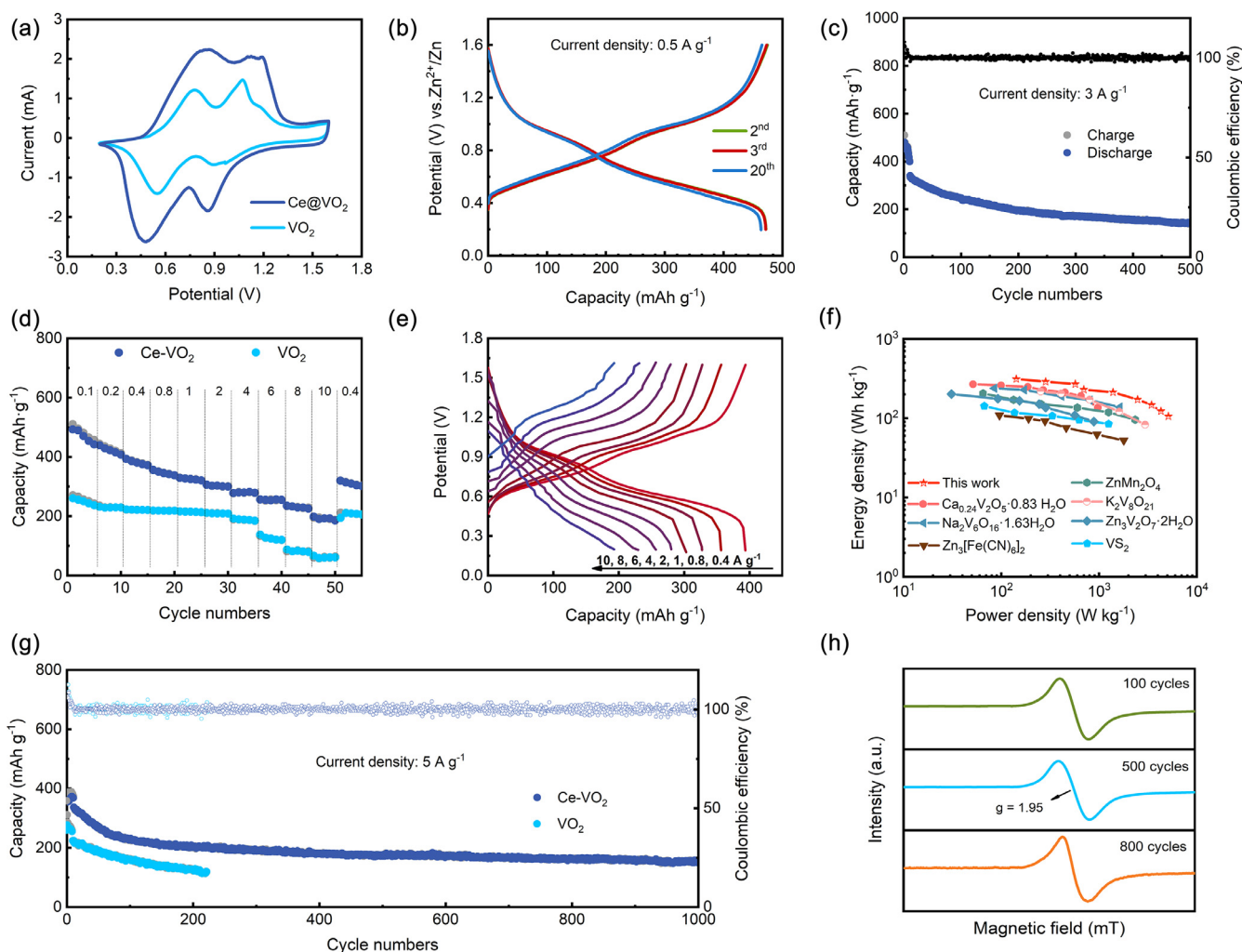


Fig. 3. (a) CV curves of Ce-VO₂ and pure VO₂ at 1 mV s⁻¹. (b) Typical charge–discharge curves of Ce-VO₂ at 0.5 A g⁻¹. (c) Cycling performance of the Ce-VO₂ electrode at the current density of 3 A g⁻¹. (d) Rate performance of the Ce-VO₂ and pure VO₂ electrodes at varied current rates. (e) GCD profiles of the Ce-VO₂ electrode at different current densities. (f) Ragone plots of the Ce-VO₂ cathode compared with other previously reported electrode materials. (g) Cycling behavior of the Ce-VO₂ and pure VO₂ electrodes at the current density of 5 A g⁻¹. (h) EPR diagram of the Ce-VO₂ electrode at different stages charging states at a current density of 5 A g⁻¹.

corresponding reduction peaks shift to lower potentials with increasing scanning speed.

The formula to explore the capacity contributions of the cells dominated by the diffusion contribution and surface-induced pseudocapacitance is $i = av^b$, which can be transformed through a logarithmic calculation into $\log i = b \log v + \log a$ (where a and b are constants; constant b with the value of 0.5–1.0 is obtained by the slope of the line of $\log v$ against $\log i$ [45]). When b is 1, the capacity of the electrode is completely controlled by the capacitance contribution, whereas when b is 0.5, the redox process is fully controlled by diffusion limitation [46]. The b values corresponding to peaks 1, 2, 3, and 4 are 0.77, 0.797, 0.801, and 0.860, respectively, which are all between 0.75 and 1.00 (Fig. 4(b)). The redox capacity is controlled by both diffusion limitation and capacitance contribution, with the latter playing a major role in the electrochemical reaction. The contribution ratio of the surface capacitance obtained from the calculations is shown in Fig. 4(c). The pseudocapacitive behavior of the batteries refers to a series of electrochemical reactions that occur on the electrode surface during charging and discharging, thereby forming an electrochemical interface on the surface of the electrochemical system. This interface has a capacitive effect and can store charge, causing the capacitor-like behavior of the battery during charging and discharging. The contributions of the surface-induced capacitance behavior

to the capacity at the scanning speed of 0.2–1.0 mV s⁻¹ is 58%, 64%, 68%, 72%, and 75%. Meanwhile, the surface-controlled contribution at the sweep rate of 1 mV s⁻¹ is displayed in Fig. 4(d) (blue area). The diffusion coefficient of Ce-VO₂ and VO₂ electrodes was obtained by GITT at the current density of 50 mA g⁻¹. As shown in Figs. 4(e)(f), the calculated diffusion coefficient of Ce-VO₂ is 10⁻⁹–10⁻¹², which is higher than that of VO₂ (10⁻¹⁰–10⁻¹⁴, Fig. S5), indicating an improvement in the ion conductivity. In addition, the diffusion coefficient slightly changes during the process because of the large specific surface area of the active material and increase in the number of active sites, thereby increasing the contact area between the electrode and electrolyte. Furthermore, when combined with the theoretical calculation results (Fig. S6), the adsorption energy of Zn²⁺ on Ce-VO₂ (–0.46 eV) is lower than that on VO₂ material (–0.59 eV), which is conducive to the reversible insertion/extraction of Zn²⁺.

3.4. Zn-ion storage mechanism of Ce-VO₂

To further elucidate the structure evolution of Ce-VO₂ cathode during repeated charging/discharging process, the ex situ XRD patterns of the electrode were analyzed at different states (Figs. 5(a)(b)). The diffraction peak at 26.8° corresponding to the (110) crystal planes shows

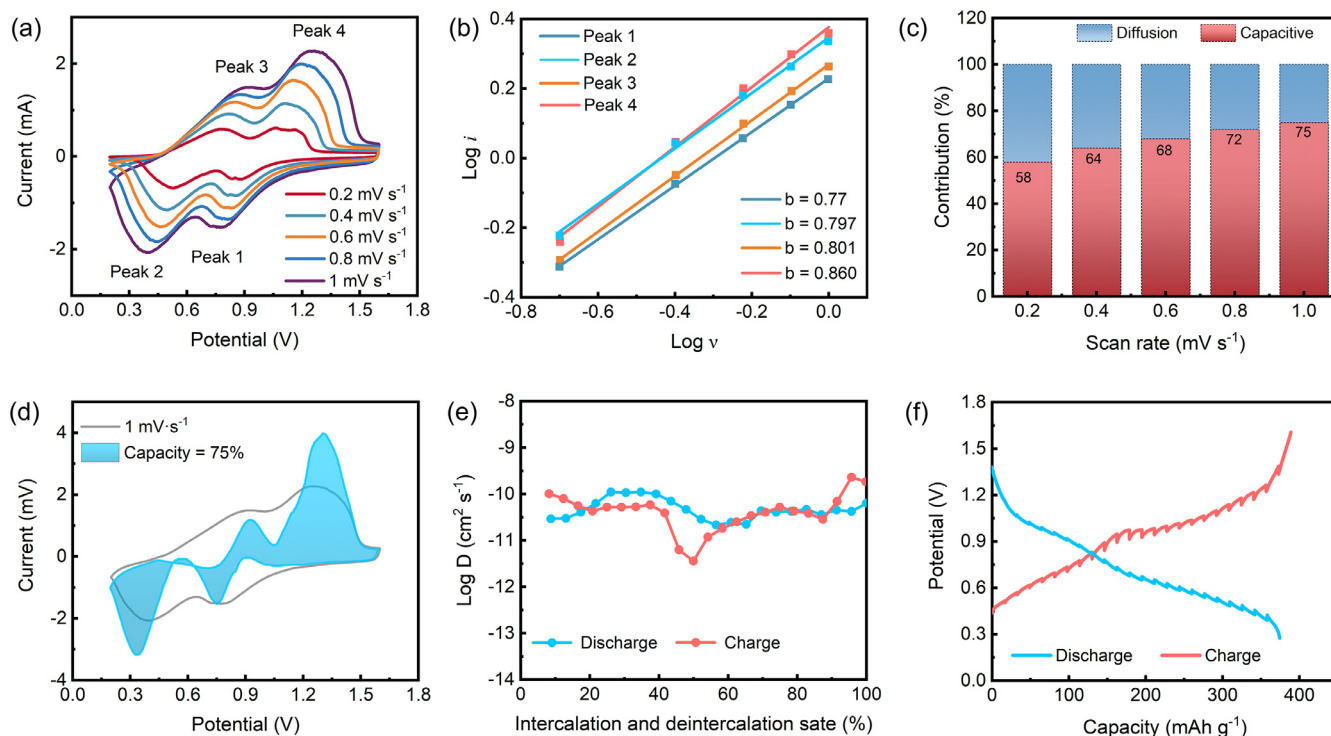


Fig. 4. (a) CV curves of Ce-VO₂ at different sweeping speeds (0.2–1.0 mV s⁻¹). (b) Linear slope obtained from the logarithm of the peak current at different sweep speeds to obtain the *b* value. (c) Capacity contribution ratio at different sweep speeds. (d) Capacitance-controlled charge contribution at the scanning speed of 1.0 mV s⁻¹. (e) Solid-phase diffusion coefficient of Zn²⁺ in the Ce-VO₂ electrode during charging and discharging. (f) Charge and discharge curves of the GITT.

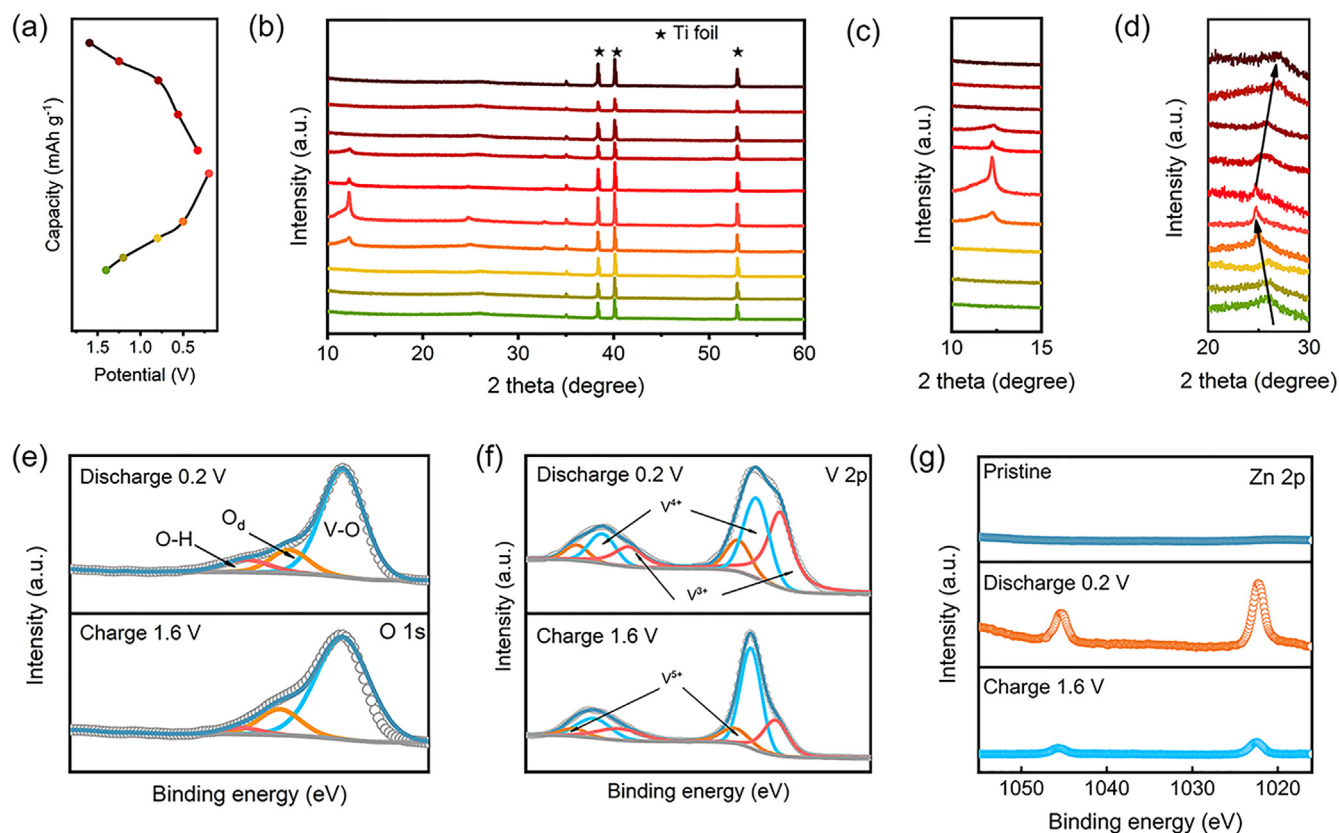


Fig. 5. (a)(b) Ex situ XRD patterns of Ce-VO₂ at different charging and discharging states. (c) XRD magnified patterns of the characteristic peak of the byproduct during charging and discharging processes. (d) XRD patterns of the (110) peaks in different states. Ex situ XPS spectra of the Ce-VO₂ electrode at its fully charged/discharged states: (e) O 1s, (f) V 2p, and (g) Zn 2p.

a slight blue shift at the beginning of the discharge (Fig. 5(d)), which is ascribed to the larger D-spacing caused by the intercalation of Zn^{2+} [47]. The diffraction peak is at the minimum 2θ position at the fully discharged state (0.2 V), indicating the maximum d-spacing. In contrast, the diffraction peaks start to shift to higher angles during charging, corresponding to the extraction of Zn^{2+} . The position of the diffraction peak still exhibits a slight blue shift upon full charging (1.6 V). The reversible extraction of a small amount of Zn^{2+} is not realized, which is one of the reasons for the capacity attenuation. The diffraction peak of the new phase appear at 12.24° (Fig. 5(c)), which is related to the by-product of $\text{Zn}_4(\text{OH})_6\text{SO}_4 \cdot 0.5\text{H}_2\text{O}$ produced at the interface between electrode and electrolyte as reported in previous works [48,49] and standard cards (Fig. S7). This phenomenon is ascribed to the gradual insertion of H^+ into the Ce-VO₂ during discharging, and the reaction of excess OH^- in the electrolyte with ZnSO_4 to form the by-product ($3x\text{Zn}^{2+} + x\text{ZnSO}_4 + 6x\text{OH}^- + 0.5x\text{H}_2\text{O} \leftrightarrow x\text{Zn}_4(\text{OH})_6\text{SO}_4 \cdot 0.5\text{H}_2\text{O}$). The intensity of the characteristic peak of the by-product reached its maximum in the fully charged state; however, this peak disappears when charged to 1.6 V. The reversible deposition/decomposition of $\text{Zn}_4(\text{OH})_6\text{SO}_4 \cdot 0.5\text{H}_2\text{O}$ indicates the excellent reversibility of the battery system. Therefore, $\text{H}^+/\text{Zn}^{2+}$ intercalation/deintercalation ($(y - 3x)\text{Zn}^{2+} + 6x\text{H}^+ + 2ye^- + \text{Ce-VO}_2 \leftrightarrow \text{Ce-H}_{6x}\text{Zn}_{y-3x}\text{VO}_2$) is the Zn storage mechanism of the entire system.

The ex situ XPS spectra for each representative state were used to analyze the valence state of the active material. Specifically, from the XPS results of the O 1s spectra (Fig. 5(e)), the higher relative content of O–H can be attributed to the insertion of H^+ when the cathode is charged to 0.2 V compared to the fully charged state. Moreover, the intensity of V^{4+} decreased with increasing V^{3+} content during discharging because of the intercalation of Zn^{2+} according to the V 2p spectra (Fig. 5(f)). Simultaneously, the various valence states of V gradually approach the original state as the charging process progresses. The reversible transformation of the vanadium valence states verifies the structural stability of the Ce-VO₂ electrodes. In addition, no obvious signals of Zn 2p are detected in the original XPS results (Fig. 5(g)). However, two prominent signal peaks at 1045.2 and 1022.3 eV in the fully discharged state of the Zn 2p spectrum (Fig. 5(g)), indicating the successful insertion of Zn^{2+} . The XPS results for charging to 1.6 V didn't return to the original state owing to the failure extraction of a small number of Zn^{2+} [50]. Furthermore, the reaction has minimal influence on the morphology of Ce-VO₂ (Fig. S8), indicating a stable structure that ensures prolonged cycling stability and excellent rate performance.

4. Conclusions

Ce-VO₂ nanostrips were designed and prepared with oxygen vacancies generated during their synthesis according to the test results. Ce-VO₂ was used as the active material to assemble CR2016 aqueous Zn-ion button batteries based on 2 M ZnSO_4 aqueous solution as the electrolyte. A series of structural characterization tests, including SEM, TEM, XPS and BET, confirmed the nanostructure of the Ce-VO₂ material with a large specific surface area and pore volume, which increased the contact area between the active material and electrolyte and shortened the transfer and diffusion distance of Zn^{2+} . Combined with the theoretical calculation results, the co-existence of exogenous elements and oxygen vacancies improved the conductivity of the electrode material and weakened the interaction between the host and guest ions. Meanwhile, lowered R_{ct} and a higher solid-phase diffusion coefficient denote the improved surface activity of the electrode and promoted the diffusion transfer kinetics of the ions and electrons, thereby promoting the rate and cyclic performance of the electrode. Such structural modifications of the material and the prospect of enhancing the conductivity by doping with rare-earth metals and introducing oxygen vacancies are important factors for improving the stability of V-based oxides in AZIBs.

Declaration of Competing Interest

Shenglin Xiong is a guest editor for special issue: Energy Material Chemistry, and was not involved in the editorial review or the decision to publish this article. All authors declare that there are no competing interests.

CRediT authorship contribution statement

Mingying Bao: Writing – original draft. **Zhengchunyu Zhang:** Writing – review & editing. **Xuguang An:** Writing – review & editing. **Baojuan Xi:** Writing – review & editing. **Shenglin Xiong:** Writing – review & editing, Formal analysis, Conceptualization.

Acknowledgements

This work was supported by the National Natural Science Foundation of China (U21A2077), Natural Science Foundation of Shandong Province (ZR2021ZD05), and Taishan Scholars Program of Shandong Province (ts20190908).

Supplementary materials

Supplementary material associated with this article can be found, in the online version, at doi:10.1016/j.chphma.2024.05.004.

References

- [1] Y. Wu, K. Zhang, S. Chen, Y. Liu, Y. Tao, X. Zhang, Y. Ding, S. Dai, Proton inserted manganese dioxides as a reversible cathode for aqueous Zn-ion batteries, *ACS Appl. Energy Mater.* 3 (2020) 319–327.
- [2] P. He, Q. Chen, M. Yan, X. Xu, L. Zhou, L. Mai, C.W. Nan, Building better zinc-ion batteries: A materials perspective, *EnergyChem* 1 (2019) 100022.
- [3] A. Tang, C. Wan, X. Meng, X. Li, X. Hu, M. Huang, X. Ju, Oxygen vacancies confined in porous $\text{Co}_3\text{V}_2\text{O}_8$ sheets for durable and high-energy aqueous sodium-ion capacitors, *Nano Res.* 15 (2022) 5123–5133.
- [4] H. Liu, J.G. Wang, W. Hua, Z. You, Z. Hou, J. Yang, C. Wei, F. Kang, Boosting zinc-ion intercalation in hydrated MoS_2 nanosheets toward substantially improved performance, *Energy Storage Mater.* 35 (2021) 731–738.
- [5] Y. Niu, Z. Yu, Y. Zhou, J. Tang, M. Li, Z. Zhuang, Y. Yang, X. Huang, B. Tian, Constructing stable Li-solid electrolyte interphase to achieve dendrites-free solid-state battery: A nano-interlayer/Li pre-reduction strategy, *Nano Res.* 15 (2022) 7180–7189.
- [6] N. Zhang, Y. Dong, M. Jia, X. Bian, Y. Wang, M. Qiu, J. Xu, Y. Liu, L. Jiao, F. Cheng, Rechargeable aqueous Zn–V₂O₅ battery with high energy density and long cycle life, *ACS Energy Lett.* 3 (2018) 1366–1372.
- [7] Y. Liu, J. Wang, J. Sun, F. Xiong, Q. Liu, Y. An, L. Shen, J. Wang, Q. An, L. Mai, A glutamate anion boosted zinc anode for deep cycling aqueous zinc ion batteries, *J. Mater. Chem. A* 10 (2022) 25029–25038.
- [8] H. Lu, X. Zhang, M. Luo, K. Cao, Y. Lu, B.B. Xu, H. Pan, K. Tao, Y. Jiang, Amino acid-induced interface charge engineering enables highly reversible Zn anode, *Adv. Funct. Mater.* 31 (2021) 2103514.
- [9] W. Gou, H. Chen, Z. Xu, Y. Sun, X. Han, M. Liu, Y. Zhang, High specific capacity and mechanism of a metal–organic framework-based cathode for aqueous zinc-ion batteries, *Energy Adv.* 1 (2022) 1065–1070.
- [10] B. Tang, L. Shan, S. Liang, J. Zhou, Issues and opportunities facing aqueous zinc-ion batteries, *Energy Environ. Sci.* 12 (2019) 3288–3304.
- [11] Y. Yang, Y. Tang, G. Fang, L. Shan, J. Guo, W. Zhang, C. Wang, L. Wang, J. Zhou, S. Liang, Li^+ intercalated $\text{V}_2\text{O}_5 \cdot n\text{H}_2\text{O}$ with enlarged layer spacing and fast ion diffusion as an aqueous zinc-ion battery cathode, *Energy Environ. Sci.* 11 (2018) 3157–3162.
- [12] M. Liao, J. Wang, L. Ye, H. Sun, Y. Wen, C. Wang, X. Sun, B. Wang, H. Peng, A deep-cycle aqueous zinc-ion battery containing an oxygen-deficient vanadium oxide cathode, *Angew. Chem. Int. Ed.* 59 (2020) 2273–2278.
- [13] Z. Zhang, B. Xi, X. Ma, W. Chen, J. Peng, S. Xiong, Recent progress, mechanisms, and perspectives for crystal and interface chemistry applying to the Zn metal anodes in aqueous zinc-ion batteries, *SusMat* 2 (2022) 114–141.
- [14] Y. Liu, S. Guo, W. Ling, M. Cui, H. Lei, J. Wang, W. Li, Q. Liu, L. Cheng, Y. Huang, In-situ oriented oxygen-defect-rich MnNO via nitridation and electrochemical oxidation based on industrial-scale Mn_2O_3 to achieve high-performance aqueous zinc ion battery, *J. Energy Chem.* 76 (2023) 11–18.
- [15] Y. Tong, Y. Zang, S. Su, Y. Zhang, J. Fang, Y. Yang, X. Li, X. Wu, F. Chen, J. Hou, M. Luo, Methylene blue intercalated vanadium oxide with synergistic energy storage mechanism for highly efficient aqueous zinc ion batteries, *J. Energy Chem.* 77 (2023) 269–279.
- [16] N. Zhang, X. Chen, M. Yu, Z. Niu, F. Cheng, J. Chen, Materials chemistry for rechargeable zinc-ion batteries, *Chem. Soc. Rev.* 49 (2020) 4203–4219.

- [17] Z. Zhang, P. Wang, C. Wei, J. Feng, S. Xiong, B. Xi, Synchronous regulation of D-band centers in Zn substrates and weakening Pauli repulsion of Zn ions using the ascorbic acid additive for reversible zinc anodes, *Angew. Chem. Int. Ed.* 63 (2024) e202402069.
- [18] X. Wang, K. Feng, B. Sang, G. Li, Z. Zhang, G. Zhou, B. Xi, X. An, S. Xiong, Highly reversible zinc metal anodes enabled by solvation structure and interface chemistry modulation, *Adv. Energy Mater.* 13 (2023) 2301670.
- [19] C. Guo, S. Yi, R. Si, B. Xi, X. An, J. Liu, J. Li, S. Xiong, Advances on defect engineering of vanadium-based compounds for high-energy aqueous zinc-ion batteries, *Adv. Energy Mater.* 12 (2022) 2202039.
- [20] H. Lu, Z. Zhang, X. An, J. Feng, S. Xiong, In situ electrochemically transforming VN/V₂O₃ heterostructure to highly reversible V₂NO for excellent zinc ion storage, *Small Struct.* 4 (2023) 2300191.
- [21] P. Yadav, N. Kumari, A.K. Rai, A review on solutions to overcome the structural transformation of manganese dioxide-based cathodes for aqueous rechargeable zinc ion batteries, *J. Power Sources* 555 (2023) 232385.
- [22] Y.Y. Liu, T.T. Lv, H. Wang, X.T. Guo, C.S. Liu, H. Pang, Nsutite-type VO₂ microcrystals as highly durable cathode materials for aqueous zinc-ion batteries, *Chem. Eng. J.* 417 (2021) 128408.
- [23] Y. Liu, X. Wu, Review of vanadium-based electrode materials for rechargeable aqueous zinc ion batteries, *J. Energy Chem.* 56 (2021) 223–237.
- [24] Y. Zhou, F. Chen, H. Arandiyani, P. Guan, Y. Liu, Y. Wang, C. Zhao, D. Wang, D. Chu, Oxide-based cathode materials for rechargeable zinc ion batteries: Progresses and challenges, *J. Energy Chem.* 57 (2021) 516–542.
- [25] X. Fan, X. Wen, Y. Tang, W. Zhou, K. Xiang, H. Chen, β -VO₂/carbon nanotubes core-shelled microspheres and their applications for advanced cathode in aqueous zinc ion batteries, *Electrochim. Acta* 400 (2021) 139425.
- [26] M. Yang, Y. Wang, Z. Sun, H. Mi, S. Sun, D. Ma, P. Zhang, Anti-aggregation growth and hierarchical porous carbon encapsulation enables the C@VO₂ cathode with superior storage capability for aqueous zinc-ion batteries, *J. Energy Chem.* 67 (2022) 645–654.
- [27] X. Dai, F. Wan, L. Zhang, H. Cao, Z. Niu, Freestanding graphene/VO₂ composite films for highly stable aqueous Zn-ion batteries with superior rate performance, *Energy Storage Mater.* 17 (2019) 143–150.
- [28] F. Gao, H. Gao, K. Zhao, X. Cao, J. Ding, S. Wang, Tungsten-oxygen bond pre-introduced VO₂(B) nanoribbons enable fast and stable zinc ion storage ability, *J. Colloid Interface Sci.* 629 (2023) 928–936.
- [29] M. Li, J. Mou, L. Zhong, T. Liu, Y. Xu, W. Pan, J. Huang, G. Wang, M. Liu, Porous ultrathin W-doped VO₂ nanosheets enable boosted Zn²⁺ (de)intercalation kinetics in VO₂ for high-performance aqueous Zn-ion batteries, *ACS Sustain. Chem. Eng.* 9 (2021) 14193–14201.
- [30] M. Bao, Z. Zhang, X. An, J. Liu, J. Feng, B. Xi, S. Xiong, Introducing Ce ions and oxygen defects into V₂O₅ nanoribbons for efficient aqueous zinc ion storage, *Nano Res.* 16 (2023) 2445–2453.
- [31] D. Zhang, J. Cao, Y. Yue, T. Pakornchote, T. Bovornratanaraks, J. Han, X. Zhang, J. Qin, Y. Huang, Two birds with one stone: Boosting zinc-ion insertion/extraction kinetics and suppressing vanadium dissolution of V₂O₅ via La³⁺ incorporation enable advanced zinc-ion batteries, *ACS Appl. Mater. Interfaces* 13 (2021) 38416–38424.
- [32] L. Xie, W. Xiao, X. Shi, J. Hong, J. Cai, K. Zhang, L. Shao, Z. Sun, VO₂·0.26H₂O nanobelts@reduced graphene oxides as cathode materials for high-performance aqueous zinc ion batteries, *Chem. Commun.* 58 (2022) 13807–13810.
- [33] H. He, D. Huang, Q. Gan, J. Hao, S. Liu, Z. Wu, W.K. Pang, B. Johannessen, Y. Tang, J.L. Luo, H. Wang, Z. Guo, Anion vacancies regulating endows MoSSe with fast and stable potassium ion storage, *ACS Nano* 13 (2019) 11843–11852.
- [34] Y. Zeng, Z. Lai, Y. Han, H. Zhang, S. Xie, X. Lu, Oxygen-vacancy and surface modulation of ultrathin nickel cobaltite nanosheets as a high-energy cathode for advanced Zn-ion batteries, *Adv. Mater.* 30 (2018) 1802396.
- [35] W. Xu, C. Liu, Q. Wu, W. Xie, W.Y. Kim, S.Y. Lee, J. Gwon, A stretchable solid-state zinc ion battery based on a cellulose nanofiber–polyacrylamide hydrogel electrolyte and a Mg_{0.23}V₂O₅·1.0H₂O cathode, *J. Mater. Chem. A* 8 (2020) 18327–18337.
- [36] Q. Li, X. Ye, Y. Jiang, E.H. Ang, W. Liu, Y. Feng, X. Rui, Y. Yu, Superior potassium and zinc storage in K-doped VO₂(B) spheres, *Mater. Chem. Front.* 5 (2021) 3132–3138.
- [37] H. Chen, T. Liu, J. Mou, W. Zhang, Z. Jiang, J. Liu, J. Huang, M. Liu, Free-standing N-self-doped carbon nanofiber aerogels for high-performance all-solid-state supercapacitors, *Nano Energy* 63 (2019) 103836.
- [38] L.F. Chen, Z.H. Huang, H.W. Liang, W.T. Yao, Z.Y. Yu, S.H. Yu, Flexible all-solid-state high-power supercapacitor fabricated with nitrogen-doped carbon nanofiber electrode material derived from bacterial cellulose, *Energy Environ. Sci.* 6 (2013) 3331–3338.
- [39] P. He, M. Yan, G. Zhang, R. Sun, L. Chen, Q. An, L. Mai, Layered VS₂ nanosheet-based aqueous Zn ion battery cathode, *Adv. Energy Mater.* 7 (2017) 1601920.
- [40] L. Zhang, L. Chen, X. Zhou, Z. Liu, Towards high-voltage aqueous metal-ion batteries beyond 1.5 V: The zinc/zinc hexacyanoferrate system, *Adv. Energy Mater.* 5 (2015) 1400930.
- [41] C. Xia, J. Guo, Y. Lei, H. Liang, C. Zhao, H.N. Alshareef, Rechargeable aqueous zinc-ion battery based on porous framework zinc pyrovanadate intercalation cathode, *Adv. Mater.* 30 (2018) 1705580.
- [42] N. Zhang, F. Cheng, Y. Liu, Q. Zhao, K. Lei, C. Chen, X. Liu, J. Chen, Cation-deficient spinel ZnMn₂O₄ cathode in Zn(CF₃SO₃)₂ electrolyte for rechargeable aqueous Zn-ion battery, *J. Am. Chem. Soc.* 138 (2016) 12894–12901.
- [43] G. Li, Z. Yang, Y. Jiang, C. Jin, W. Huang, X. Ding, Y. Huang, Towards polyvalent ion batteries: A zinc-ion battery based on NASICON structured Na₃V₂(PO₄)₃, *Nano Energy* 25 (2016) 211–217.
- [44] B. Tang, G. Fang, J. Zhou, L. Wang, Y. Lei, C. Wang, T. Lin, Y. Tang, S. Liang, Potassium vanadates with stable structure and fast ion diffusion channel as cathode for rechargeable aqueous zinc-ion batteries, *Nano Energy* 51 (2018) 579–587.
- [45] K. Zhu, T. Wu, K. Huang, A high-capacity bilayer cathode for aqueous Zn-ion batteries, *ACS Nano* 13 (2019) 14447–14458.
- [46] D. Zhao, X. Wang, W. Zhang, Y. Zhang, Y. Lei, X. Huang, Q. Zhu, J. Liu, Unlocking the capacity of vanadium oxide by atomically thin graphene-analogous V₂O₅·nH₂O in aqueous zinc-ion batteries, *Adv. Funct. Mater.* 33 (2023) 2211412.
- [47] Z. Zhang, B. Xi, X. Wang, X. Ma, W. Chen, J. Feng, S. Xiong, Oxygen defects engineering of VO₂·xH₂O nanosheets via in situ polypyrrole polymerization for efficient aqueous zinc ion storage, *Adv. Funct. Mater.* 31 (2021) 2103070.
- [48] Z. Li, S. Ganapathy, Y. Xu, Z. Zhou, M. Sarilar, M. Wagemaker, Mechanistic insight into the electrochemical performance of Zn/VO₂ batteries with an aqueous ZnSO₄ electrolyte, *Adv. Energy Mater.* 9 (2019) 1900237.
- [49] L. Chen, Z. Yang, Y. Huang, Monoclinic VO₂(D) hollow nanospheres with super-long cycle life for aqueous zinc ion batteries, *Nanoscale* 11 (2019) 13032–13039.
- [50] N. Liu, X. Wu, L. Fan, S. Gong, Z. Guo, A. Chen, C. Zhao, Y. Mao, N. Zhang, K. Sun, Intercalation pseudocapacitive Zn²⁺ storage with hydrated vanadium dioxide toward ultrahigh rate performance, *Adv. Mater.* 32 (2020) 1908420.